Synthesis, structural characterization and optical properties of multilayered Yttria-stabilized ZrO_2 thin films obtained by aerosol assisted chemical vapour deposition

P. Amézaga-Madrid. W. Antúnez-Flores, I. Monárrez-García, J. González-Hernández, R. Martínez-Sánchez, M. Miki-Yoshida

Abstract

Multilayered Yttria-stabilized zirconium (YSZ) oxide thin films were synthesized by aerosol assisted chemical vapour deposition onto borosilicate glass substrate. The film consisted of a periodic stack of several YSZ layer pairs. Each pair was composed of layers, a few nanometers thick, of the same composition but different density. Optically the multilayered microstructure correspond to alternating layers of high (dense layer) and low (porous layer) refraction index. The microstructure was analysed by electron and atomic force microscopy. Optical properties were evaluated by reflectance spectroscopy, and associated with the cross sectional microstructure of the films. The measured effective refractive index of the films deviates from bulk value. The discrepancy can be explained by the multilayered structure of the film.

Keywords: Multilayered films, YSZ, TEM, Optical properties

Introduction

Zirconium oxide (ZrO_2) is an important material, which finds numerous applications. Films of this material have received considerable attention owing to their interesting properties such as high melting point (3133 K), high refractive index over the full visible range, oxidation resistance and thermodynamic stability over a very wide temperature range [1,2]. ZrO_2 has in addition high ionic conductivity with poor electronic

conductivity [3]. Because of these properties, ZrO_2 is used as electrolyte membranes for micro-scale solid-oxide fuel cells for portable power generation [4] and switchable mirrors [5], also in laser mirrors, and optical coatings such as interference filters [2,6,7]. On the other hand, multilayer films have been extensively used in soft X-ray optics, such as mirrors [8], optical devices [9], band pass filters, beam splitters etc. [10]. Many techniques have been employed to produce Yttria-stabilized zirconium (YSZ) coatings including chemical vapor deposition [11] and some variation of it such as aerosol assisted chemical vapour deposition (AACVD) [12–14], sol–gel [15], electron beam deposition [16], radio frequency and direct current reactive magnetron sputtering [17], as well as reactive evaporation [18]. Among these techniques, AACVD has proved to be a simple, reproducible and inexpensive method to produce thin films. In addition, the method can be applied to cover large areas as well as to the inside wall of tubes [19].

In this work, we report the fabrication of submicron, multilayered, nanocrystalline YSZ thin films, with different refractive indices obtained by simply altering the processing conditions of the AACVD system. The multilayer is a periodic stack of two YSZ layers with different density, the low density layer be existent due to the presence of voids. Optically, this multilayered structure is equivalent to a periodic stack of one high refractive index and one low refractive index layer. Changing the deposition parameters we can change the thickness of each layer and the density of the porous layer, then with the process reported here, we are able to control the optical properties of the multilayered film. This flexibility allows the use of a single material in a variety of devices. Processing parameters such as those that determine the impact of the precursor droplet with the substrate were used to modify the structure of the

multilayered films, and therefore to control optical constants such as refractive index and optical absorption. Variations in transmittance and reflectance of multilayered films were usually done by changing the film thickness [20–24]; in this work, we have used changes in the refractive index of individual layers to produce multilayered films with different optical properties. A qualitative correlation between the microstructure and the optical properties of polycrystalline YSZ films was described. The films were characterized by X-ray diffraction (XRD), scanning electron microscopy (SEM), transmission electron microscopy (TEM) and scanning probe microscopy (SPM). Optical properties were analyzed by reflectance spectroscopy.

Experimental details

YSZ thin films were obtained onto borosilicate 7059 (2.5×7.5 cm^2) glass substrates by AACVD technique, details of the experimental set up have been described before [25]. The starting solution was a dilution of Zr acetylacetonate (0.083 mol dm^{-3}) and Y acetate (0.017 mol dm^{-3}) in methanol (99.9% pure). The optimum substrate temperature was found to be of 723±1 K. The carrier gas was micro-filtered air at a fixed pressure of 310 kPa. The aerosol was generated by an ultrasonic nebulizer Sonaer model PG-241 working at 2.4 MHz. This aerosol was directed towards the substrate by a nozzle, which has a periodic movement at constant velocity to scan the whole surface of the substrate. All the films were obtained with a velocity of the nozzle of ~0.5 mm s^{-1}. To show the influence of the movement in the microstructure of the films, sample G was obtained with a static nozzle, it was deposited in two steps of 15 min each, with a waiting interval of 5 min between them. For the other samples, the total number of steps (number of layers) was varied in order to obtain films of different

thickness; the total deposition time was also recorded. To analyze the influence of aerosol droplet velocity near to the substrate into the growing characteristics and microstructure of the films, we have varied several deposition parameters, such as, the carrier gas flux, the aperture at the tip of the nozzle and the distance between the nozzle and the substrate. Table 1 presents the principal preparation parameters of the samples analyzed in this report.

Crystal structure of the samples was analyzed by XRD in a Philips X-Pert system, the spectra were obtained using Cu K_α radiation (λ=0.1542 nm) at 40 keV and 30 mA. The scanning angle 2θ was varied between 15° and 80°, at 0.1° step. Surface morphology and cross sectional microstructure of the films were studied by field emission SEM using a JEOL JSM-7401F, operated at 5 kV. Cross sectional samples were studied by TEM. High resolution transmission electron microscopy (HRTEM), and selected area electron diffraction (SAED) were performed in a FEI Titan 80-300 with image Cs-corrector, at 300 kV. High angle annular dark field (HAADF) in scanning transmission electron microscopy (STEM) mode were realized in a JEOL JEM 2100F with STEM Cs-corrector, operated at 200 kV. SEM cross section samples were prepared by conventional methods in a cross section polisher JEOL SM-09010 at 5 kVand 120 µA. In addition, TEM cross section samples were prepared using a dual beam focused ion beam (FIB) FEI Nova Nanolab system, with Ga ion beam operated at 30 kV. Samples were lift out insitu by a Omniprobe 100 nanomanipulator. Elemental analysis of the films was achieved by means of energy dispersive X-ray spectroscopy (EDS), using an Oxford Inca microanalysis system attached to the electron microscopes.

Table 1
Principal preparation parameters, calculated droplet velocity and film's thickness

Sample	Air flux [L min^{-1}]	Steps	Section of nozzle [cm^2]	Distance nozzle-substrate [cm]	Droplet velocity [cm s^{-1}]	Thickness [nm]
A	6	30	1.05	1	72	435
B	5	30	1.05	1	60	350
C	4	15	1.05	1	48	143
D	5	13	1.05	2	43	93
E	5	15	1.05	3	37	160
F	6	30	1.05	1	72	363
G[a]	6	2	1.77	1.5	48	357
H	6	30	1.77	1	50	181
I	5	30	1.77	1	42	530
J	6	15	0.47	0.5	216	202
K	6	15	0.47	1	216	208
L	6	15	0.47	1.5	189	194

[a] Sample G was prepared with a static nozzle.

Atomic force microscopy (AFM) was employed to evaluate the surface of the films. Grain size and root mean square (RMS) roughness have been determined. These analyses were performed in a Veeco Multimode Nanoscope IV-a system in tapping mode, using.

Film's thickness was determined from near normal reflectance spectra, using a Filmetrics F-20 UV optical fibre reflectance spectrophotometer in contact probe mode. From these data, the refractive index of the samples was obtained.

Results and discussion

Growth characteristics: According to previous reports [25,26], the growth rate of films prepared by AACVD is influenced by several parameters, such as: precursor concentration in starting solution, substrate temperature, aerosol droplet velocity

towards the substrate (determined by the carrier gas flux, section of nozzle, distance between tip nozzle and substrate), lateral velocity of the nozzle, and those related with the aerosol generation (such as size and size distribution of droplets). In this article, we present results of films deposited fixing the following conditions: precursor concentration (0.083 mol dm^{-3} of Zr and 0.017 mol dm^{-3} of Y), substrate temperature (723 K), lateral velocity of the nozzle (~0.5 mm s^{-1}) and the aerosol generation frequency (2.4 MHz). A more complete analysis of the characteristics of films prepared using a wider range of the deposition parameters is in progress.

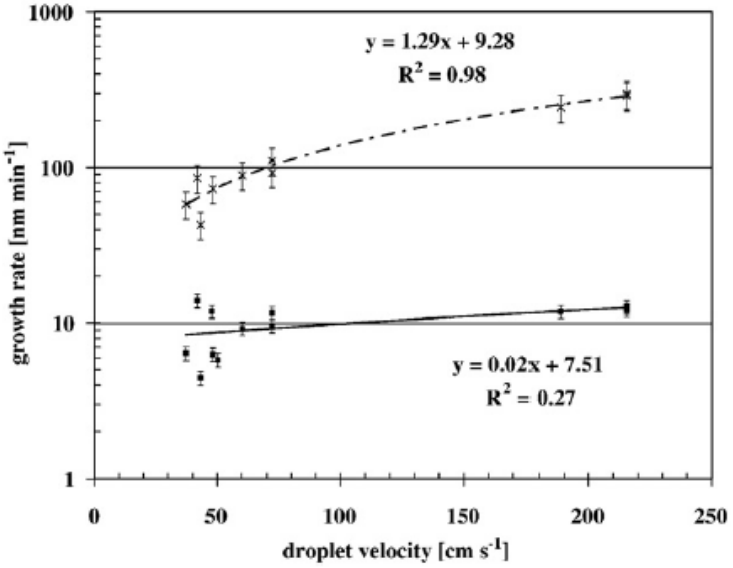

Fig. 1. Growth rate (●) and effective growth rate (×) of the films as a function of aerosol droplet velocity.

We have analyzed in detail the influence of the aerosol droplet velocity near to the substrate into the growth characteristics of the films. Table 1 presents the estimated droplet velocity, taking into account the carrier gas flux, the section of the nozzle's tip, and the distance between the tip and the surface of the substrate. As a first approximation, the aerosol droplet velocity was considered equal to that of the carrier

gas. In addition, the expansion of the carrier gas, due to its increase of temperature, as it approaches the heated substrate was not taken into account. The influence of gas expansion into the droplet velocity is similar for all the cases analyzed in this work. Additionally, to consider the effect of the distance between the nozzle's tip and the substrate, we took into account the increment of the aerosol stream section out of the nozzle. To assess this increment, the dimensions (length and width) of the aerosol stream out of each nozzle were measured experimentally as a function of the distance travelled by the stream towards the substrate. We have correlated the aerosol droplet velocity near to the surface with the growth rate, the average grain size and roughness of the films.

The growth rate of the films has been calculated in two different ways; depending on how the deposition time is defined. In one case, the deposition time was taken as the total time of aerosol injection to any section of the substrate (total spraying time). With the total spraying time, we calculated the growth rate. In the second way, an effective growth rate was determined by evaluating the time that the nozzle was injecting aerosol directly to some point on the surface, this was considered as the effective deposition time, which gave the effective growth rate. The effective deposition time was estimated considering the number of steps in the process, the displacement velocity of the nozzle, the section of the nozzle tip, and the distance between the nozzle tip and surface. Fig. 1 shows a plot of both growth rate vs. aerosol droplet velocity, as can be observed, there exists a large dispersion of the data of the growth rate, reflected by the poor linear correlation obtained (R^2 ~ 0.27). Whereas, a linear correlation (R^2 ~0.98) was observed between the effective growth rate and droplet velocity; it can be stated that the effective

growth rate increased linearly with the droplet velocity up to around 200 cm s^{-1}. Despite that the calculus of the effective deposition time was done comparatively, it provides a better estimation of the actual deposition time. The correlation between effective growth rate and droplet velocity can be justified considering that an increase of the aerosol droplet velocity toward the substrate results in a more effective adsorption of the precursor spices and attachment of the forming oxide. A more detailed simulation of the aerosol flow towards the substrate considering a distribution of the temperature is in course, particularly to asses the actual temperature of the stream near to the surface.

Microstructure: The composition of the films was studied by EDS. This analysis showed that Zr and Y in the film were almost in the same proportion than in the started solution (mol ratio Y/Zr~0.20). The homogeneity in the composition was also verified by EDS.

Fig. 2a shows the X-ray diffraction spectra of representative films analyzed in this work; they showed characteristic XRD peaks for cubic zirconia [27]. Although peak broadening prevented the confirmation of d-space parameter in YSZ relative to tetragonal zirconia, the lack of phase segregation into Y_2O_3 or other metallic elements suggests the presence of single YSZ oxide phase. Peak broadening in the spectra indicates a microstructure composed of nanocrystals, which were also observed in HRTEM and HAADF images. It is worthwhile to remark that despite the weak and wide XRD peaks, very well crystallized nanometric grains constituted the films, as it is shown in the HRTEM micrograph of sample E in Fig. 2b. Lattice fringes measurement in Fig. 2b was consistent with the interplanar distance of the YSZ cubic phase [28]. Additionally, selected area electron diffraction patterns results also confirm the

existence of the stabilized phase (see inset of Fig. 2b). The lattice parameter obtained from SAED patterns was 0.514±0.005 nm, in agreement to values reported in the literature [29] for YSZ.

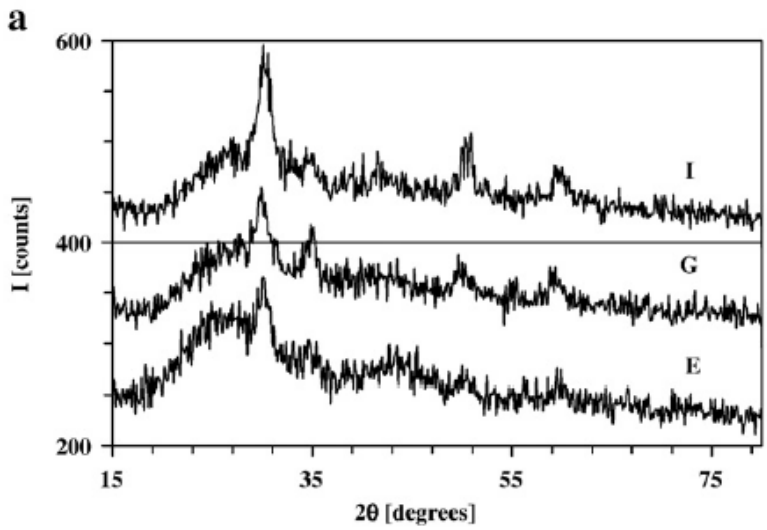

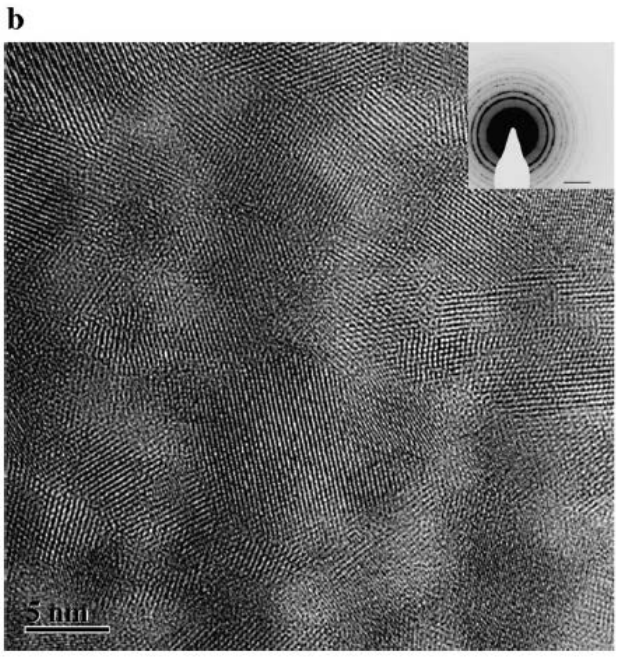

Fig. 2. a) XRD spectra of representative films E, G and I. b) Bright field HRTEM image of sample E, it is shown that the film is polycrystalline and composed by a well crystallized nanomaterial. The inset shows its corresponding SAED pattern (bar is equivalent to 4 nm^{-1}).

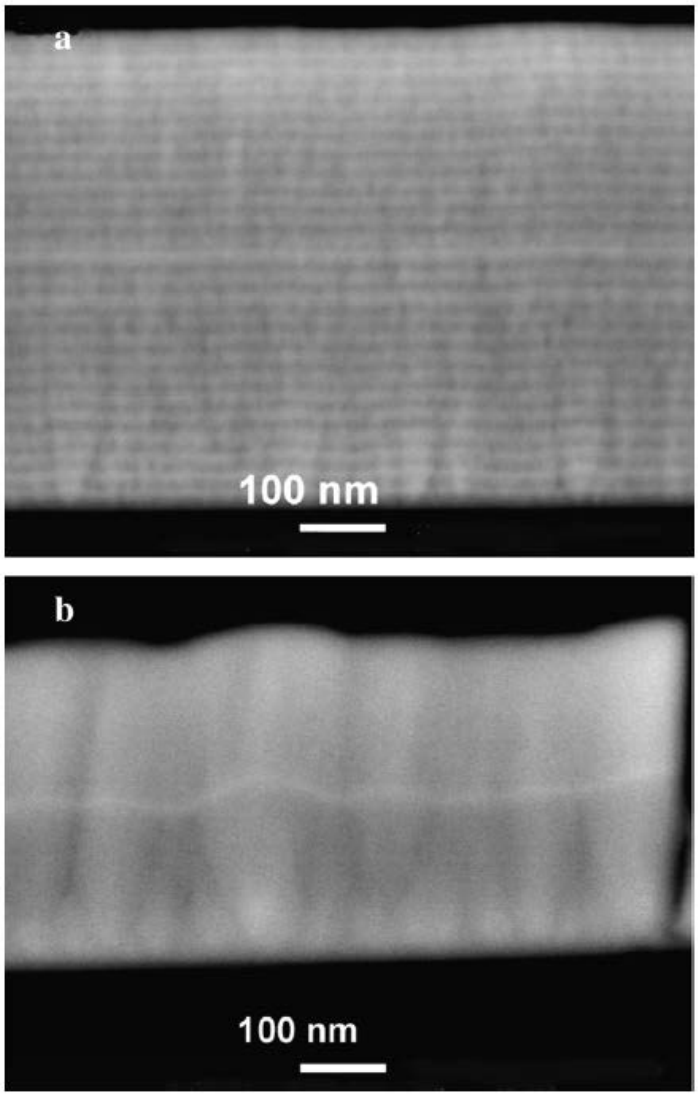

Fig. 3. Backscattered compositional SEM images of YSZ films. a) Sample I, it can be observed one layer for each spraying step. b) Sample G, it is shown only two layers.

The films showed a multilayered microstructure, as illustrated in the cross sectional SEM image of Fig. 3a, also observed in Fig. 2b. The number of layers matches with the number of spraying steps during the deposition of sample I (Fig. 3a). In contrast, sample G deposited with a static nozzle only showed two layers, one for each spraying interval (see Fig. 3b). All the experimental evidence (EDS, HRTEM,

HAADF) suggested that the layers have the same composition but different density. Therefore, in the backscattered compositional SEM image, bright layers correspond to more dense material, and dark zones correspond to the porous layers.

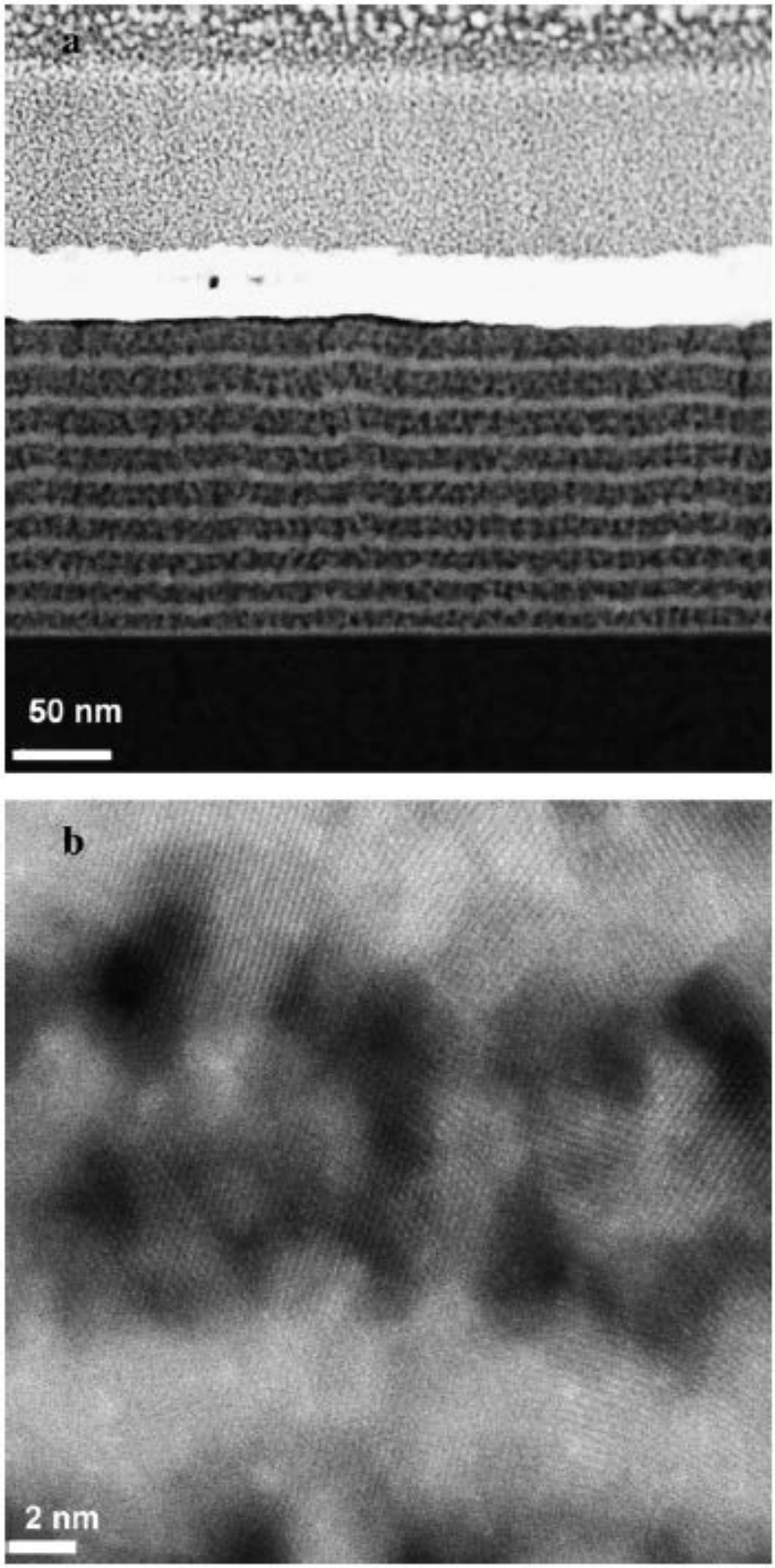

Fig. 4. HAADF STEM images of sample E. a) Overview of the cross section of the film. b) High resolution Z-contrast image showing the high density and porous layers.

Fig. 4 shows HAADF (Z contrast) STEM images of the cross section of sample E previously prepared by FIB. It is shown in Fig. 4a that the cross section of the film is composed by many layers; at the bottom the glass substrate (dark) and at the top a Cr (white) and Pt/C (bright) layers deposited to protect the film before the FIB preparation. The thickness of the dense layers was around 5 nm, whereas the porous layers had nearly 15 nm. Fig. 4b shows a high-resolution HAADF image of the same sample; it clearly shows that the microstructure of the film is constituted by a periodic juxtaposition of dense and porous layers.

The suggested explanation of the development of the multilayered microstructure is depicted in Fig. 5. We propose that the dense layer was produced locally in the portion of the substrate hit directly by the aerosol injected by the nozzle. As the nozzle sweep all the surface, the dense layer covers all the scanned regions. In the mean time, as the nozzle goes to the extreme of its movement and come back, the mist of aerosol that surround all the surface deposit gradually the porous layer around to the actual position of the nozzle.

Fig. 6 shows AFM images of samples B and E surface obtained in tapping mode. Fig. 6a presents the surface morphology of sample B, which is composed by small nanometric grains (around 20 nm). Fig. 6b shows the surface morphology of sample E; it can be observed that the film microstructure is formed by grains of size in the range of 35 to almost 100 nm. Analysis of the AFM images suggested some correlation between the grain size and the aerosol droplet velocity; i.e. the grain size decreased as the droplet velocity increased, possibly due to the break up of the droplets or precursor particles during their impact with the substrate. RMS roughness was also obtained from

the AFM study of the films. As expected, RMS roughness decreased as the grain size decreased as well. Table 2 presents the average grain size and RMS roughness of the YSZ films.

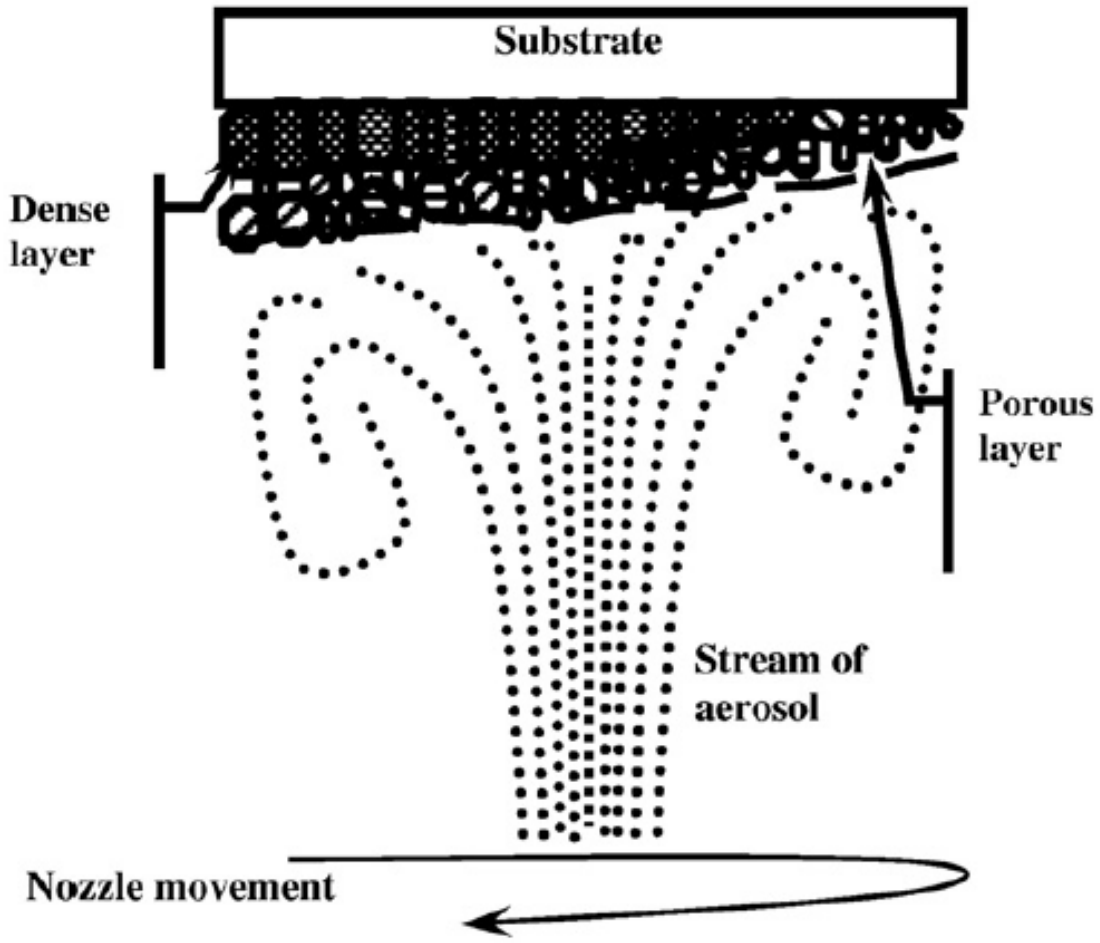

Fig. 5. Illustration of proposed multilayered film growth mechanism.

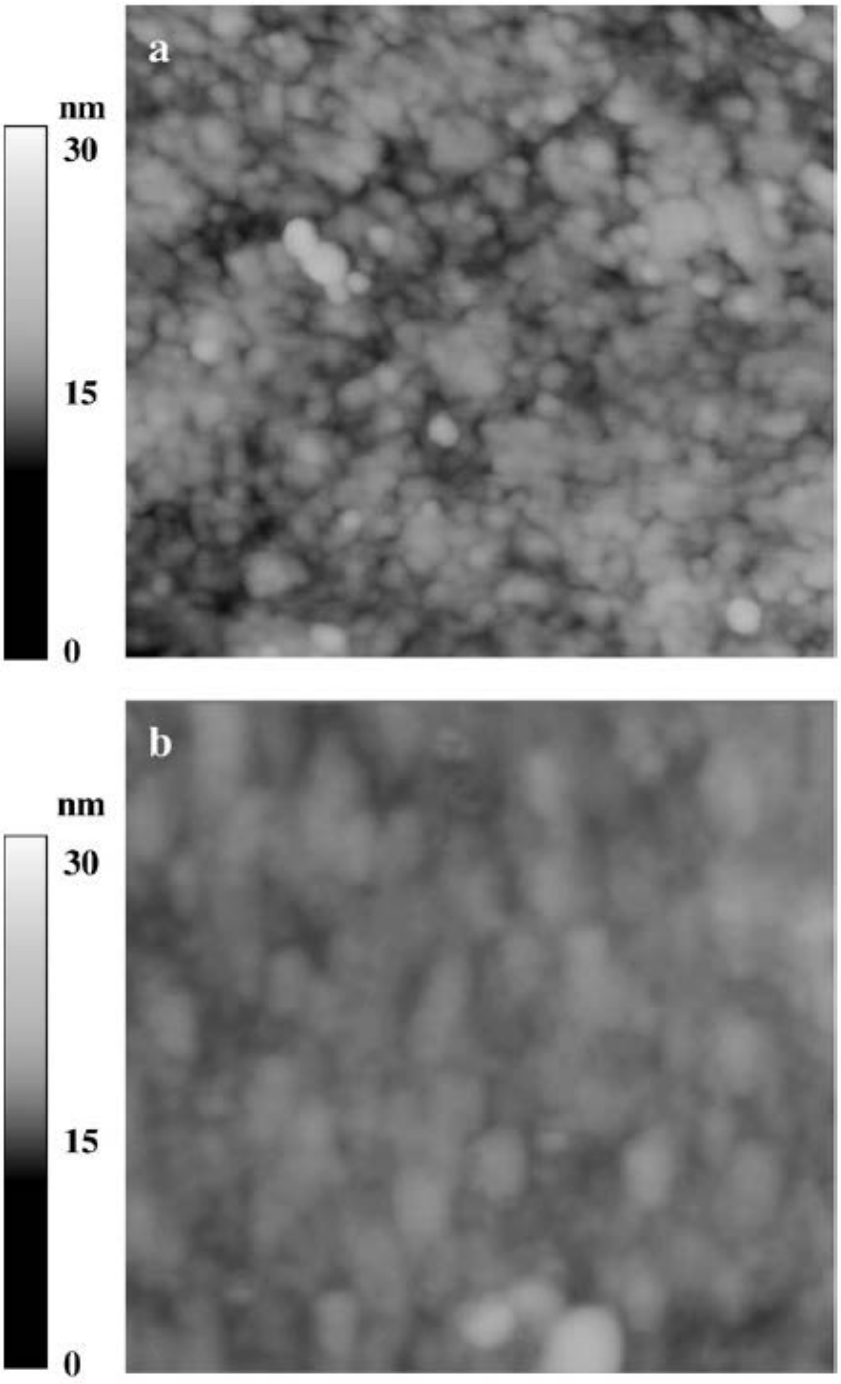

Fig. 6. Tapping mode AFM images of YSZ films. a) Sample B obtained with 30 steps and nozzle-substrate distance of 1 cm, it is composed of very small grains. b) Sample E obtained with 15 steps and nozzle-substrate distance of 3 cm, it shows bigger grains than sample B. The width of each image corresponds to 0.5 µm.

Optical properties: Fig. 7a shows the reflectance spectrum of samples E and I, all the films presented similar spectrum. The refractive index has been obtained from the analysis of the reflectance spectra using Filmeasure v2 software. Fig. 7b shows the refractive index of three different YSZ films, each of them with different microstructure, and consequently different density. Film E (shown in Fig. 4) present a periodic multilayered structure, with alternating layers of high and low density (high porosity); thus, the effective density of this film (Fig. 4a) is lower than that of film G (Fig. 3b). Therefore, the effective refractive index of film G is higher than that of film E. Sample I (see Fig. 3a), showed less porosity than film E, but more than film G; consequently it is expected to have an intermediate effective refractive index, as depicted in Fig. 7b. The dependence of refractive index and density has been reported for titania films [30].

Table 2
Average grain size and RMS roughness obtained from the analysis of AFM images

Sample	Average grain size [nm]	RMS roughness [nm]
A	19±3	0.8±0.1
B	19±3	6.3±0.7
C	45±6	2.1±1.2
D	234±29	2.1±0.6
E	35±6	3.7±0.4
F	19±7	0.7±0.1
G	160±37	4.2±0.1
H	17±3	1.2±0.3
I	433±43	3.9±0.6
J	24±5	0.9±0.1
K	19±5	0.7±0.1
L	54±9	2.9±0.6

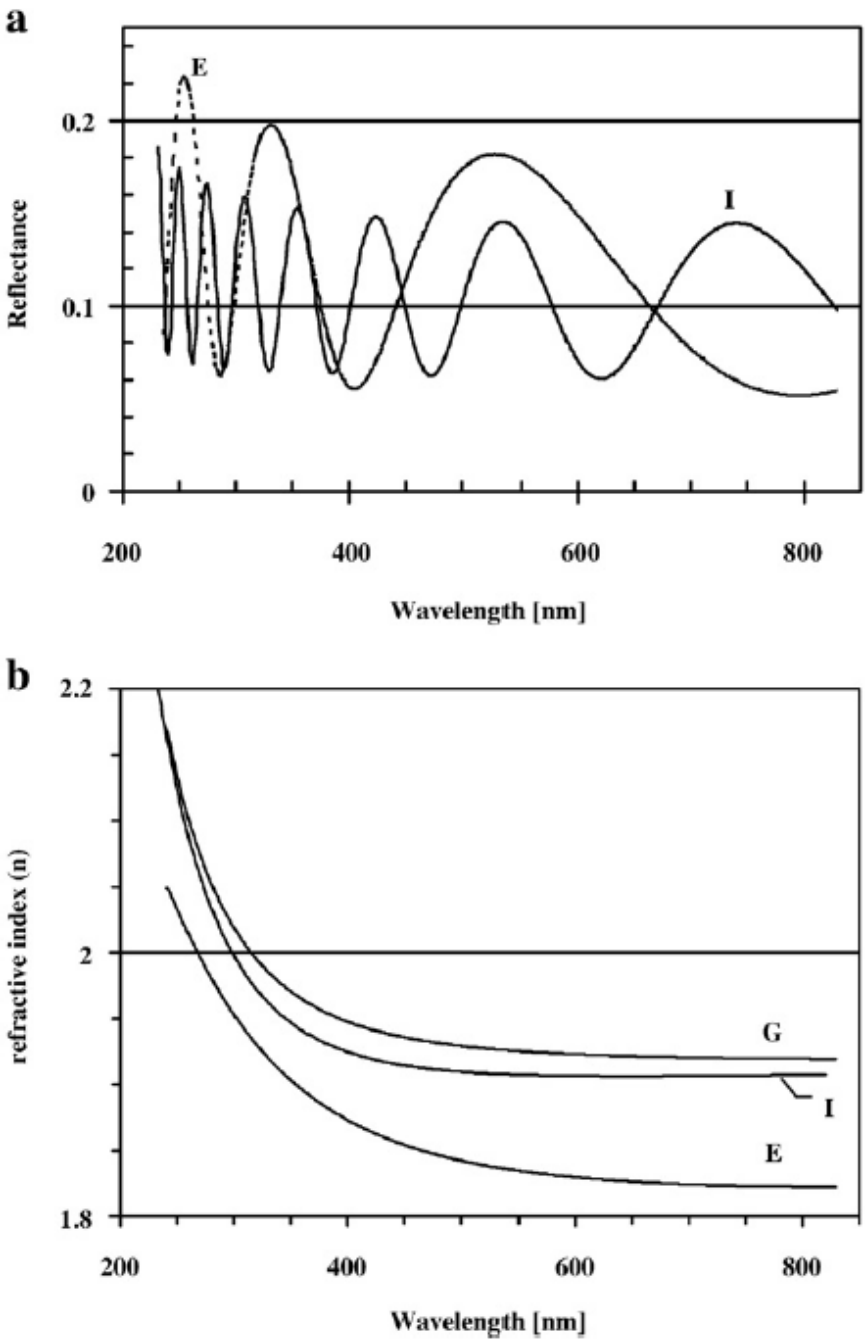

Fig. 7. a) Reflectance spectrum of samples E and I. b) Effective refractive index of three different YSZ films. It is shown the correlation between the microstructure (density) and refractive index.

Conclusions

Multilayered YSZ films were synthesized by AACVD technique, using a dilution of Zr acetyl acetonate and Y Acetate in absolute methanol. All the layers had the same composition but different density, i.e. the films are composed of a periodic intercalation of high (dense) and low (porous) refractive index layers. It is demonstrated that this AACVD technique, with a displacing nozzle, provides a powerful tool for creating a specific multilayer film structure. Our results suggest that the multilayered microstructure of the films can be tailored by a careful control of the displacement velocity of the nozzle, the velocity of the droplets towards the surface, and the way in which the droplets collide with the substrate. Effective growth rate correlated linearly with the aerosol droplet velocity; this result suggests that the strength of the collision of the droplet with the substrate affect the adhesion of material to the forming film. Refractive index can be correlated with the film microstructure, denser films have refractive index values closer to that reported for bulk.

Acknowledgements

The authors would like to thank E. Torres, J. Saenz, K. Campos, O. Solis, S. Miranda, M. Moreno and D. Lardizabal for their technical assistance. We are in debt with Application Lab. JEOL for cross section preparation, SEM and HAADF analysis. Also to Application Lab. FEI for FIB preparation, and HRTEM analysis. This work was partially supported by a grant from CONACYT SEP-47911.

References

[1] Advances in Zirconia Science and Technology, Bologna, Italy, 16–17

December 1988, in: S. Meriani (Ed.), Proceedings of the International Conference Zirconia ’88, 1989.

[2] S. Venkataraj, O. Kappertz, H. Weis, R. Drese, R. Jayavel, M. Wuttig, J. Appl. Phys. 92 (2002) 599.

[3] A.K. Jonsson, M. Strømme Mattsson, G.A. Niklasson, Lithium Batteries, Hawaii, Fall 1999, in: R.A. Marsh, Z. Ogumi, J. Prakash, S. Surampudi (Eds.), The Electrochemical Society Proceedings, 99–25, 1999, p. 504.

[4] C.D. Baertsch, K.F. Jensen, J.L. Hertz, H.L. Tuller, S.T. Vengallatore, S.M. Spearing, M.A. Schmidt, J. Mater. Res. 19 (2004) 2604.

[5] A.L. Larsson, A. Gunnar Niklasson, Sol. Energy Mater. Sol. Cells 84 (2004) 351.

[6] W.H. Lowdermilk, D. Milam, F. Rainer, Thin Solid Films 73 (1980) 155.

[7] W.T. Pawlewicz, D.D. Hays, P.M. Martin, Thin Solid Films 73 (1980) 169.

[8] J. González-Hernández, B.S. Chao, S.R. Ovshinsky, D.D. Allred, J. X-Ray Sci. Technol. 6 (1996) 1.

[9] M. Ghanashyam Krishna, A.K. Bhattacharya, Mater. Sci. Eng., B 86 (2001) 41.

[10] D. Bhattacharyya, N.K. Sahoo, S. Thakur, N.C. Das, Vacuum 60 (2001) 419.

[11] K.L. Choy, Prog. Mater. Sci. 48 (2003) 57.

[12] M. Miki-Yoshida, F. Paraguay-Delgado, W. Estrada-Lopez, E. Andrade, Thin Solid Films 376 (2000) 99.

[13] V. Brinzari, G. Korochenkov, V. Golovanov, J. Schwank, V. Lantto, S.

Saukko, Thin Solid Films, 408 (2002) 51.

[14] M. Mehdi, B. Mohagheghi, M. Shokooh-Saremi, Semicond. Sci. Technol. 19 (2004) 764.

[15] J. Zhang, L. Gao, J. Solid State Chem. 177 (2004) 1425.

[16] S. Ramamurthy, N.S. Subramanian, K. Sarangarajan, B. Santhi, Bull. Electrochem. 14 (1998) 446.

[17] P.F. Carcia, R.S. McLean, M.H. Reilly, Z.G. Li, L.J. Pillione, R.F.Messier, J. Vac. Sci. Technol. A 21 (2003) 745.

[18] J. Philip, N. Theodoropoulou, G. Berera, J.S. Moodera, B. Satpati, Appl. Phys. Lett. 85 (2004) 777.

[19] M. Miki-Yoshida, W. Antúnez-Flores, K. Gomez-Fierro, L. Villa-Pando, R. Silveyra-Morales, P. Sánchez-Santiago, R. Martínez-Sánchez, M. José-Yacamán, Surf. Coat. Technol. 200 (2006) 4111.

[20] P.J. Martin, R.P. Netterfield, in: J.J. Cuomo, S.M. Rossnagel, H.R. Kaufman (Eds.), Handbook of Ion Beam Processing Technology, Noyes, New Jersey, 1989, p. 373.

[21] E. Ritter, Appl. Opt. 20 (1981) 21.

[22] K.H. Guenther, Appl. Opt. 23 (1983) 3806.

[23] H.K. Pulker, Coatings on Glass, Thin Films Science and Technology, vol. 6, Elsevier, New York, 1984.

[24] H.A. Macleod, J. Vac. Sci. Technol. A 4 (1986) 418.

[25] F. Paraguay-Delgado, W. Estrada-Lopez, E. Andrade, M. Miki-Yoshida, Thin Solid Films 350 (1999) 192.

[26] M. Miki-Yoshida, E. Andrade, Thin Solid Films 224 (1993) 87.

[27] P.S. Patil, Mater. Chem. Phys. 59 (1999) 185.

[28] Joint Committee on Powder Diffraction Standards, Powder Diffraction File, International Center for Diffraction Data, Swarthmore, PA, (1996), card 30-1468.

[29] R.H. French, S.J. Glass, F.S. Ohuchi, Y.N. Xu, W.Y. Ching, Phys. Rev. B: Condens. Matter 49 (1994) 5133.

[30] C.R. Ottermann, K. Bange, Thin Solid Films 286 (1996) 32.